Measurement of neutron energy spectra for E_g=23.1 and 26.6 MeV mono-energetic photon induced reaction on ^{nat}C using laser electron photon beam at NewSUBARU

Toshiro Itoga[1,*], *Hiroshi* Nakashima[2,4], *Toshiya* Sanami[2,3,6], *Yoshihito* Namito[3,6], *Yoichi* Kirihara[3], *Shuji* Miyamoto[5], *Akinori* Takemoto[5], *Masashi* Yamaguchi[5] and *Yoshihiro* Asano[2,5]

[1]JASRI, 1-1-1, Kouto, Sayo-cho, Sayo-gun, Hyogo 679-5198, Japan
[2]RIKEN SPring-8 Center, 1-1-1, Kouto, Sayo-cho, Sayo-gun, Hyogo 679-5198, Japan
[3]KEK, 1-1, Oho, Tsukuba-shi, Ibaraki 305-0801, Japan
[4]JAEA, 2-4 Shirakata, Tokai-mura, Naka-gun, Ibaraki 319-1195, Japan
[5]LASTI University of Hyogo, 3-1-2 Koto, Kamigori-cho, Ako-gun, Hyogo 678-1205, Japan
[6]The Graduate University for Advanced Studies (SOKENDAI), 1-1 Oho, Tsukuba, Ibaraki 305-0801, Japan

Abstract. Photo-neutron energy spectra for E_g=23.1 and 26.6 MeV mono-energetic photons on ^{nat}C were measured using laser Compton scattering facility at NewSUBARU BL01. The photon energy spectra were evaluated through measurements and simulations with collimator sizes and arrangements for the laser electron photon. The neutron energy spectra for the ^{nat}C(g,xn) reaction were measured at 60 degrees in horizontal and 90 degrees in horizontal and vertical with respect to incident photon. The spectra show almost isotropic angular distribution and flat energy distribution from detection threshold to upper limit defined by reaction Q-value.

1 Introduction

In the shielding design of electron accelerator facilities, the double differential cross-section (DDX) data, which fully describe energy and angle of emitted particles, of the photo-neutron production reaction are necessary in order to determine thicknesses and layouts of shielding wall with considering neutron transport and penetration. Especially, the data for materials consisting of collimator, target and beam dump are quite important because of continuous beam loss during operation. Graphite is one of the materials due to relatively low neutron yield, long radiation length and high melting point.

Until now, there are few experimental data of photo-neutron production DDX since there were no facilities providing intense mono-energetic photons for the experiment. Only the total photo-neutron production cross-section data have been provided so far even in giant resonance energy region, mainly for a physical interest on nuclear structure [1].

Thus, neutrons having Maxwellian energy and isotropic angular distribution are assumed in the shielding design. This assumption will be adequate for relatively heavy nuclei [2], however should be confirmed experimentally for light nuclei due to less population of nucleus. For carbon photo neutron reaction, Noda et al. pointed out that an isospin selection rule affects energy dependence of total cross section [3]. Experimental DDX data on carbon are highly desired to confirm these points.

Recently, the laser electron photon beam facilities are in operation using a laser Compton backscattering (LCS) technique in the world. At NewSUBARU BL01 [4], mono-energetic photon up to 75 MeV is obtained by appropriate combinations of the electron beam energy, laser wave-length and collimators. The variable energy, intense monochromatic photon source is useful to measure the DDX data.

In this paper, we present the spectral measurements and simulations for the circular polarized laser electron photon beam and photo-neutron at NewSUBARU BL01. Measurements and simulations were performed to evaluate energy spectrum of LCS photon. Measurements were performed to obtain the photo-neutron energy spectrum and the angular distribution for 23.1 and 26.6 MeV gamma induced reaction on graphite. In addition, the target activity was also measured in order to confirm the absolute yields of the neutron.

2 Experiments

Figure 1 shows the experimental set-up at NewSUBARU BL01. The laser electron photon beam is generated by backward Compton scattering of laser photon. The maximum photon energies of 23.1 and 26.6 MeV are obtained for 1149 and 1223 MeV electrons, respectively, with Nd:YVO_4 laser (1064 nm). Circular polarization was chosen by using a $\lambda/4$ wave plate to avoid influence

* Corresponding author: itoga@spring8.or.jp

from polarization [5]. The two 100 mm thick lead collimators with the aperture diameters of 3 and 2 mm were set at 15.6 and 18.5 m from scattering point. By defining scattering angle using the collimators the nominal energy spreads of photon were estimated to be 1.2 and 1.6 MeV. A cylindrical graphite target, 100 mm long × 10 mm in diameter (1.92 g/cm^3) was set at 26 m away from the laser scattering point.

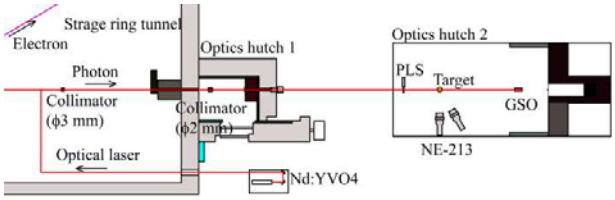

Figure 1. Schematic view of NewSUBARU BL01. PLS indicate the plastic scintillation detector.

The photon and neutron measurements were carried out in the optics hutch 2. The absolute intensity and energy width of the photon were measured using a Ce:Gd_2SiO_5 (GSO) scintillator with the size of H76 × W76 × L180 mm [6]. Photon intensity was monitored by a thin plastic scintillation detector (5 mm in thickness) during the neutron measurements.

Three NE-213 organic liquid scintillators with the size of 127 mm in diameter × 127 mm long were set at the 709, 647 and 659 mm from the target, The detector position with respect to the photon beam direction were 60 and 90 degrees in horizontal direction and 90 degrees in vertical direction. Neutron energy was determined by the time-of-flight method using a single electron bunch ring operation and pulsed laser (25 kHz) in order to avoid the frame overlap and mitigate Bremsstrahlung photons.

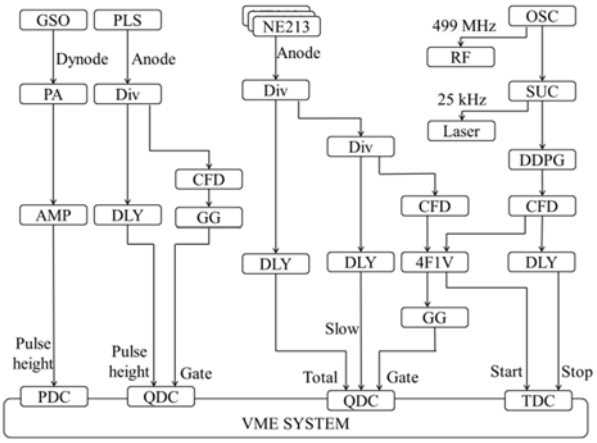

Figure 2. Block diagram of the photon and neutron measurement circuit. PLS: plastic scintillation detector, PA: preamplifier, AMP: amplifier, Div: signal divider, DLY: nano second delay, CFD: constant fraction discriminator, GG: gate generator, OSC: oscillator, SUC: synchronous universal counter, DDPG: digital delay pulse generator, 4F1V: 4 fold 1 veto, PDC: peak sensing analogue to digital converter, QDC: charge integrating analogue to digital converter, TDC: time to digital converter.

The electronic circuits show in fig. 2 was used for the photon and neutron measurements. By using QDC, the charge of the total and slow (decay) components of the anode signals were integrated for the discrimination between neutron and photon events. The neutron flight time was measured by TDC. The pulse height information of the PLS was also digitized by using QDC. These digital data were stored in a personal computer via VME system. The history of photon beam intensity for activation analysis was also recorded using PLS signals.

After the neutron measurements, the activities of ^{11}C accumulated in each targets were measured by detecting 511 keV annihilation gamma-rays with a high-pure Ge detector (ORTEC GEM20P4-70) and a multi-channel analyzer in order to confirm the absolute yields of the neutron. The dead times during the gamma-ray counting were less than 1 %.

3 Data analysis

Time of flight spectra were deduced for the neutron events identified by the pulse shape discrimination technique and converted into energy spectra. The lower energy threshold was set based on pulse height of ^{137}Cs, ^{60}Co, ^{22}Na Compton edge [7]. Figure 3 shows the neutron detection efficiency used in this data analysis. The neutron detection efficiency of the NE-213 scintillator was obtained by the calculation with SCINFUL-QMD code [8] for the energy region above 3 MeV. For the energy region up to 3 MeV, the neutron detection efficiency obtained experimentally by using a ^{252}Cf neutron source with the NBS spectrum [5]. The difference of detection efficiency was caused by the characteristics of the detectors and the distances between the target and the detectors. Finally, the energy spectra were normalized by the solid angle and the number of incident photons. In the neutron measurements, the time average of the photon intensity was 2.4 x 10^5 photons/s on the target with the laser power of 26.9 W.

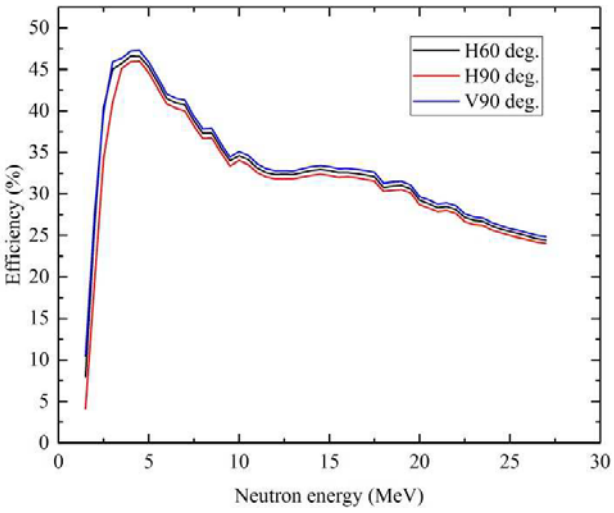

Figure 3. Neutron detection efficiency of NE-213 scintillation detector.

The activation cross sections were esitmated by considering the peak counts of gamma-ray spectra, the

peak efficiency of the high-pure Ge detector calculated by the EGS5 code [9] and the beam fluctuation during the irradiation. The activation cross sections corrected for the beam fluctuation are given as following equation.

$$\sigma = \frac{\lambda C}{N\varepsilon\gamma}\left(\sum_{i=1}^{n} N_i\right)^{-1}\left\{e^{-\lambda t_c}\left(1-e^{-\lambda t_m}\right)\right\}^{-1} \quad (1)$$

where,

$$N_i = \frac{\varphi_i}{\Delta t}\left\{\left(1-e^{-\lambda\,\Delta t}\right)e^{-\lambda(n-i)\Delta t}\right\}$$

λ is a decay constant, C is a net counts of gamma-ray peak area, N is a number of atoms in the target, ε is a peak efficiency, γ is a branching ration of gamma-ray, t_c is a cooling time, t_m is a measurement time, ϕ_i is a number of photons for iradiation time interval Δt.

In the simulation using EGS5 code, the energy of the laser electron photon E_γ was defined by the flowing equations [10].

$$E_\gamma = \frac{E_L(\beta cos\alpha+1)}{1-\beta cos\theta+\frac{E_L}{\gamma m_e c^2}\{1+\cos(\alpha+\theta)\}} \quad , \quad (2)$$

where γ is the Lorentz factor of the electron, E_L is the energy of the laser photons, $\beta=v/c$ (v is the electron velocity and c is the speed of light), α is the angle between the electron beam and laser photon direction, θ is the photon emission angle respect to the direction of the electron beam and $m_e c^2$ is the electron rest mass. The angler distribution of the laser electron photon was obtained as

$$\frac{d\sigma}{d\Omega} = \frac{\beta(sin\theta-sin\alpha)+sin(\alpha+\theta)}{\gamma^2(1+\beta cos\alpha)(1-\beta cos\theta)^2 sin\theta}\frac{r_0^2}{2}R^2\left(R+\frac{1}{R}-1+cos^2\Theta_{ER}\right), \quad (3)$$

where

$$\frac{1}{R} = 1+\frac{\gamma(1+\beta cos\alpha)E_L}{m_e c^2}(1+cos\Theta_{ER}),$$

$$\cos\Theta_{ER} = \frac{1+\cos(\alpha+\theta)}{\gamma^2(1+\beta cos\alpha)(1-\beta cos\theta)}-1,$$

r_0 is the classical electron radius [10]. The simulation results were normalized by the peak count of the experimental results. The collimator hole sizes and positions, and energy spread, beam size and divergence of electron beam were taken into account in the simulation. Electron beam parameters considering in the simulation were listed in table 1.

Table 1. Electron beam parameters in the simulation.

Maximum photon energy	23.1 MeV	26.6 MeV
Beam energy	1149 MeV	1233 MeV
Holizontal beam size (σ)	283 μm	304 μm
Vertical beam size (σ)	58.4 μm	62.68 μm
Holizontal angular divergence (σ)	277 μrad	298 μrad
Vertical angular divergence (σ)	9.1 μrad	9.8 μrad
Energy spread	0.047%	0.047%

4 Results and discussion

4.1 Photon spectrum and pulse height spectrum of GSO detector

Figure 4 shows the photon energy spectrum on the target obtained by the simulation. According to this calculation, we estimated that the energy spreads for the 23.1 and 26.6 MeV photons were 1.29 and 1.69 MeV in FWHM, if the collimators were placed at appropriate positions.

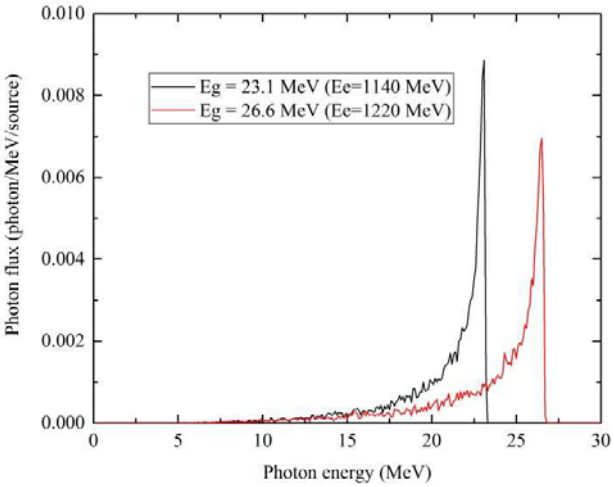

Figure 4. Simulation results of energy spectrum of the laser electron photon induced on the target for 1149 and 1233 MeV electron with 1064 nm laser photon, 3 mm and 2 mm collimators.

Figure 5 shows the measured pulse height spectrum of the GSO detector in comparison with the simulation result obtained by EGS5 code. Energy calibration of the GSO detector was determined using peak energy of the laser electron photon of the simulation result. The energy resolution of 5.0% and 6.0% at 23.1 and 26.6 MeV respectively for the GSO detector were estimated from experimental results. In the lower energy region, the simulation results show high intensity rather than the experimental data. One of the reasons of this difference is an overestimation of angular divergence of the electron beam.

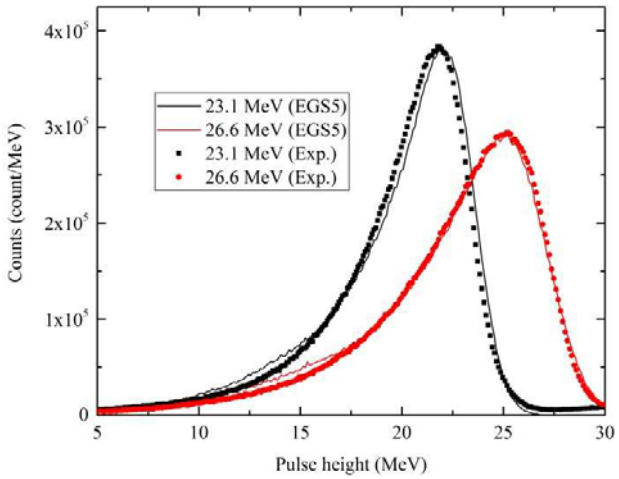

Figure 5. Pulse height spectra of GSO detector at 23.1 and 26.6 MeV in comparison with simulation result by ES5 code.

4.2 Neutron energy spectrum

Figure 6 shows the neutron energy spectra at E_g=23.1 and 26.6 MeV from the ^{nat}C(g, xn) reaction above 1.75 MeV with the simulation results of the PHITS2.82 [11]. In the fig. 6, the error bars are considered with statistical errors, the errors of the neutron detection efficiency (5%) [12] and the errors of the number of photon (5%). The photon energy spectra in fig. 5, the graphite target and NE-213 detector were considered in the simulation.

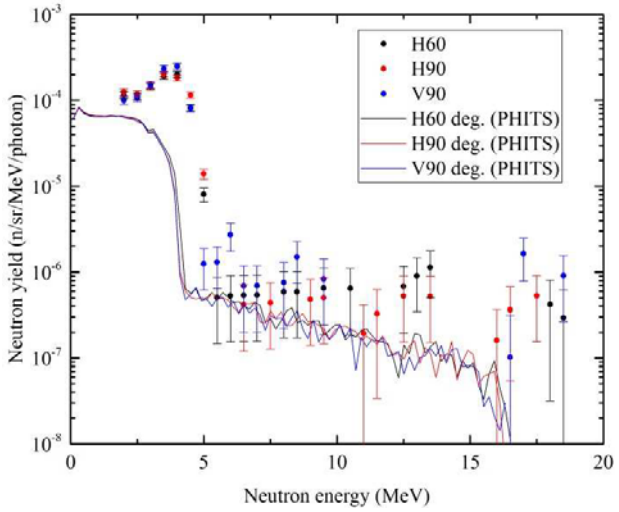

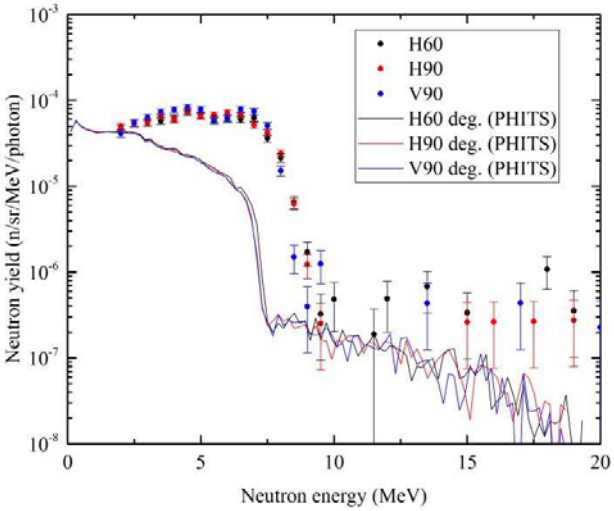

Figure 6. Neutron energy spectra produced by 23.1 MeV (top) and 26.6 MeV (bottom) quasi-mono-energetic photons in comparison with the simulation results by PHITS code. H indicates the horizontal direction and V indicates the vertical direction with respect to the direction of laser electron photons.

In the case of the detector at H60 degree, the energy resolution is less than 17.4% because of relatively short flight path. The neutrons from the ^{12}C(g, n) reaction are dominant even for low reaction Q value (-18.7 MeV). Above 4 and 8 MeV, a few events which seem to the neutrons from the ^{13}C(g, n) reaction (Q-value = -4.95 MeV) were observed. The spectra show similar shapes each other for all the angles as expected, however, their energy dependencies are different from Maxwelian distribution. The simulation results are smaller than the experimental data especially around the maximum neutron energy from the ^{12}C(g, n) reaction.

The neutron yields were compensated for the neutron attenuation in the graphite target in order to clarify neutron angular distribution. The attenuation coefficient f was obtained by following equation.

$$f = \exp\left(-\frac{\rho N_A}{m}\sigma t\right), \qquad (4)$$

where ρ is the target density, N_A is the Avogadro constant, m is the atomic weight, σ is the neutron total cross section and t is the neutron path length in the target. The JENDL-4.0 library [13] was referred to as obtain the total neutron cross section.

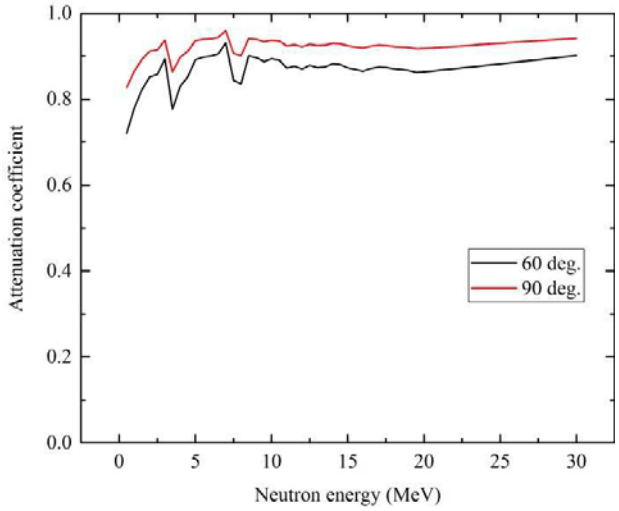

Figure 7. Neutron attenuation coefficients in the graphite target.

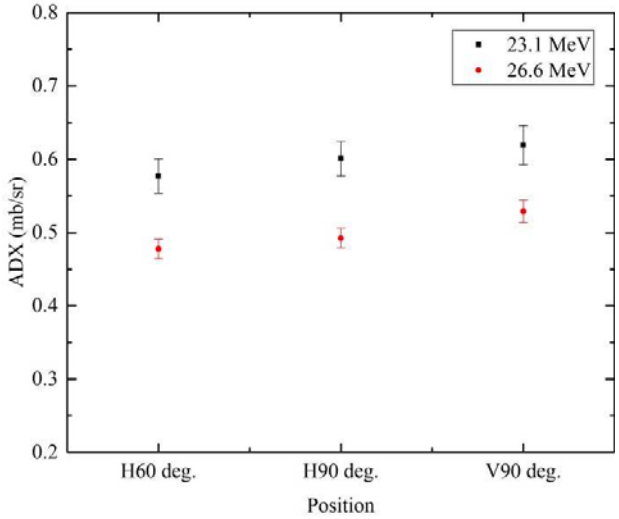

Figure 8. Neutron angular differential cross section (ADX) for ^{nat}C(g,xn) reaction.

Figure 7 shows the calculated neutron attenuation coefficients in the graphite target. The path lengths are 5.8 and 5.0 mm for 60 degree and 90 degree respectively assuming that the neutrons were produced at centre of the target. After the compensation, the neutron energy spectra were integrated above 1.75 MeV with dividing number of carbon nuclei in the target. Figure 8 shows neutron angular differential cross section (ADX) for the ^{nat}C(g, xn) reaction.

The neutron yield distribution shows nearly isotropic above 1.75 MeV. Production cross sections for the neutrons above the detection threshold (E_n > 1.75 MeV) were deduced from an average of three positions. Figure 9 shows the neutron production cross section for the ^{nat}C(g, xn) reaction in comparison with the result of PHITS code. The simulation with the mono-energetic photon also counted number of neutrons the energy of which is above 1.75 MeV. The simulation results are smaller than the experimental results.

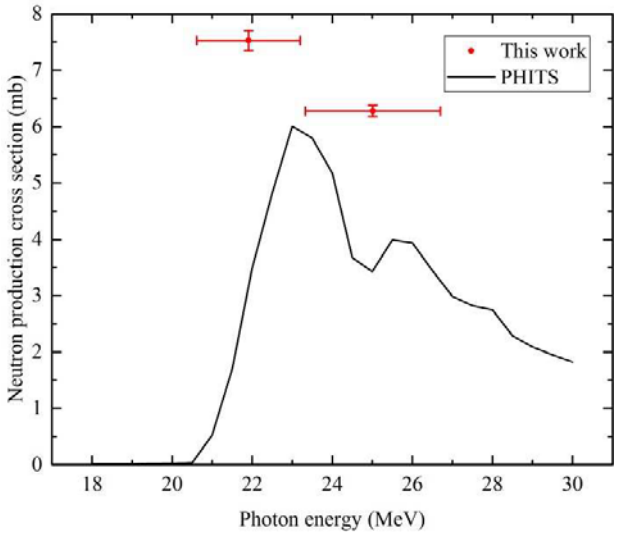

Figure 9. Neutron production cross section above E_n > 1.75 MeV with the results of PHITS calculation. The energy of this work means the centroid of the laser electron photon spectrum. Error bars of energy indicate the energy spread of the laser electron photon.

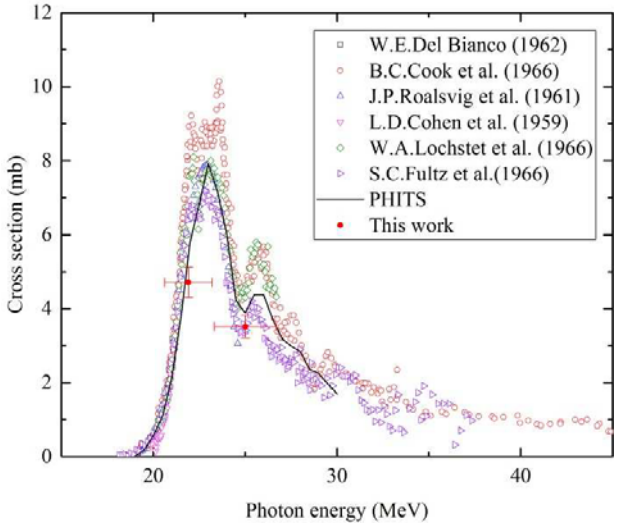

Figure 10. Comparison with other experimental data of the ^{12}C(g, n)^{11}C reaction. The energy of this work means the centroid of the laser electron photon spectrum. Error bars of energy indicate the energy spread of the laser electron photon.

4.3 Activation cross section

Figure 10 shows the activation cross sections for the ^{12}C(g,n)^{11}C reaction at E_g = 23.1 and 26.6 MeV in comparison with other experimental data [1, 14-18] and the simulation results of the PHITS code with mono-energetic photon. The produced ^{11}C nuclei in the target were counted in the simulation. The present data are close to other experimental data and simulation results.

5 Conclusions

The spectral measurements and simulations have been carried out for the circular polarized laser electron photon beam and photo-neutron at NewSUBARU BL01.

From experimental results, the energy resolutions of GSO detector were estimated 5% and 6% for 23.1 and 26.6 MeV quasi-mono-energetic photon respectively. The simulation results for the pulse height distribution of GSO scintillation detector with these energy resolutions were in good agreement with the experimental data.

Using this quasi-mono-energetic photon source, the neutron energy spectra for the $^{nat}C(g,xn)$ reaction with respect to the neutron emission angle were measured with the time-of-flight technique above 1.75 MeV. The spectra show nearly isotropic distribution and the present data were larger than the simulation results using PHITS code. On the contrary, the results of activation cross section for the $^{12}C(g,n)^{11}C$ reaction were smaller than the simulation result. Further analysis is necessary to reversal reason of this discrepancy for both experimental and calculation.

References

1. S. C. Fultz, J. T. Caldwell, B. L. Berman, R. L. Bramblett and R. R. Harvey, Phys. Rev., **143**, 790 (1965)
2. V. V. Verbinski and W. R. Burrus, Phys. Rev., **177**, 1661 (1969)
3. S. Noda, S. Hashimoto, T. Sato, T. Fukahori, S. Chiba and K. Niita, Nucl. Sci. and Tech., **52**, 57 (2015)
4. Y. Asano, S. Miyamoto and LEPS-II collaboration, Prog. Nucl. Sci. Tech., **4** 252 (2014)
5. Y. Kirihara, T. Itoga, T. Sanami, H. Nakashima, Y Namito, S. Miyamoto, A. Takemoto, M. Yamaguchi and Y. Asano, in this proceedings
6. K. Horikawa, S. Miyamoto, S. Amano and T. Mochizuki, Nucl. Instr. and Meth. A, **618** 209 (2010)
7. K. Shin, H. Tokumaru, M. Yoshida and T. Hyodo, Mem. Fac. Eng. Kyoto Univ., **41**, 116 (1979)
8. D. Satoh, S. Kunieda, Y. Iwamoto, N. Shigyo and K. Ishibashi, Nucl. Sci. Tech., **2** 657 (2002)
9. H. Hirayama, Y. Namito, A.F. Bielajew, S.J. Wilderman and W.R. Nelson, SLAC-R-730, KEK Report 2005-8 (2005)
10. Y. Taira, M. Adachi, H. Zen, T. Tanikawa, M. Hosokawa, Y. Takashima, N. Yamamoto, K. Soda and M. Katoh, Nucl. Instr. and Meth. A, **637** S116 (2011)
11. T. Sato, K. Niita, N. Matsuda, S. Hashimoto, Y. Iwamoto, S. Noda, T. Ogawa, H. Iwase, H. Nakashima, T. Fukahori, K. Okumura, T. Kai, S. Chiba, T. Furuta and L. Sihver, J.Nucl.Sci.Technol. **50**, 913 (2013).
12. S. Meigo, Nucl. Instr. and Meth. A, **401**, 365 (1997)
13. K. Shibata, O. Iwamoto, T. Nakagawa, N. Iwamoto, A. Ichihara, S. Kunieda, S. Chiba, K. Furutaka, N. Otuka, T. Ohsawa, T. Murata, H. Matsunobu, A. Zukeran, S. Kamada, and J. Katakura, J. Nucl. Sci. Technol. **48**, 1 (2011).
14. W. E. Del Bianco and W. E. Stephens, Phys. Rev., **126**, 709 (1962)
15. B. C. Cook, J. E. E. Baglin, J. N. Bradford and J. E. Griffin, Phys. Rev. **143**, 724 (1966)
16. J. P. Roalsvig, I. C. Gupta and R. H. H. Haslam, Can. J. Phys., **39**, 643 (1961)
17. L. D. Cohen and W. E. Stephens, Phys. Rev. Lett., **2**, 263 (1959)
18. W. A. Lochstet and W. E. Stephens, Phys. Rev., **141**, 1002 (1966)